The Cryosphere Discuss., 9, 5137–5169, 2015
www.the-cryosphere-discuss.net/9/5137/2015/
doi:10.5194/tcd-9-5137-2015

The Cryosphere Discussions
Open Access

Radiative transfer model for contaminated slabs: experimental validations

F. Andrieu[1,2], F. Schmidt[1,2], B. Schmitt[3], S. Douté[3], and O. Brissaud[3]

[1]Université Paris-Sud, Laboratoire GEOPS, UMR8148, 91405 Orsay, France
[2]CNRS, 91405 Orsay, France
[3]Institut de Planétologie et d'Astrophysique de Grenoble, 38041 Grenoble, France

Received: 15 July 2015 – Accepted: 6 September 2015 – Published: 29 September 2015

Correspondence to: F. Andrieu (francois.andrieu@u-psud.fr)

Published by Copernicus Publications on behalf of the European Geosciences Union.

Abstract

This article presents a set of spectro-goniometric measurements of different water ice samples and the comparison with an approximated radiative transfer model. The experiments were done using the spectro-radiogoniometer described in Brissaud et al. (2004). The radiative transfer model assumes an isotropization of the flux after the second interface and is fully described in Andrieu et al. (2015).

Two kinds of experiments were conducted. First, the specular spot was closely investigated, at high angular resolution, at the wavelength of 1.5 µm, where ice behaves as a very absorbing media. Second, the bidirectional reflectance was sampled at various geometries, including low phase angles on 61 wavelengths ranging from 0.8 to 2.0 µm.

In order to validate the model, we made qualitative tests to demonstrate the relative isotropization of the flux. We also conducted quantitative assessments by using a Bayesian inversion method in order to estimate the parameters (e.g., sample thickness, surface roughness) from the radiative measurements only. A simple comparison between the retrieved parameters and the direct independent measurements allowed us to validate the model.

We developed an innovative Bayesian inversion approach to quantitatively estimate the uncertainties in the parameters avoiding the usual slow Monte Carlo approach. First we built lookup tables, and then we searched the best fits and calculated a posteriori density probability functions. The results show that the model is able to reproduce the geometrical energy distribution in the specular spot, as well as the spectral behavior of water ice slabs. In addition, the different parameters of the model are compatible with independent measurements.

TCD
9, 5137–5169, 2015

1 Introduction

Various species of ices are present throughout the solar system, from water ice and snow on Earth to nitrogen ice on Triton (Zent et al., 1989), not to forget carbon dioxide ice on Mars (Leighton and Murray, 1966). Ice- and snow-covered areas have a strong impact on planetary climate dynamics, as they can lead to significant regional-scale albedo changes at the surface and surface–atmosphere volatiles interactions. The physical properties of the cover also have an impact on the energy balance: for example, the albedo depends on the grain size of the snow (Dozier et al., 2009; Negi and Kokhanovsky, 2011), on the roughness of the interface (Lhermitte et al., 2014), on the presence or not and the physical properties of impurities (Dumont et al., 2014), or on the specific surface area (Picard et al., 2009; Mary et al., 2013). The study and monitoring of theses parameters is a key to constraining the energy balance of a planet.

Radiative transfer models have proven essential for retrieving such properties and their evolution at a large scale, and different families exist. Ray-tracing algorithms, such as those described in Picard et al. (2009) for snow or Pilorget et al. (2013) for compact polycrystalline ice, simulate the complex path of millions of rays into the surface. They provide very accurate simulations but have the weakness of being time consuming. Analytical solutions of the radiative transfer in homogeneous granular media have been developed, for example, by Shkuratov et al. (1999) and Hapke (1981). They are fast, but when the surface cannot be described as homogeneous, they must be combined with another family of techniques such as discrete ordinate methods like DISORT (Stamnes et al., 1988). These methods have been widely studied on Earth snow (Carmagnola et al., 2013; Dozier et al., 2009; Dumont et al., 2010; Painter and Dozier, 2004) and other planetary cryospheres (Appéré et al., 2011; Eluszkiewicz and Moncet, 2003), modeling a granular surface. Compact polycrystalline ices have, however, been recognized to exist on several objects: CO_2 on Mars (Kieffer and Titus, 2001; Eluszkiewicz et al., 2005), N_2 on Triton and Pluto (Zent et al., 1989; Eluszkiewicz and Moncet, 2003) and probably SO_2 on Io (Eluszkiewicz and Moncet, 2003), owing to the very long light

TCD
9, 5137–5169, 2015

path lengths measured, over several decimeters. Radiative transfer is different in compact slabs or in granular media. We developed an approximated model (Andrieu et al., 2015) designed to study contaminated ice slabs, with a fast numerical implementation, which has already been numerically validated. The main objective of the model is the analysis of massive spectro-imaging planetary data of these surfaces. For this purpose, it is semi-analytic and quickly implemented. It is designed to retrieve the variations of thickness and impurity content of compact polycrystalline planetary ices.

In the present article, we will test the accuracy of this approximated model on laboratory spectroscopic measurements of pure water ice bidirectional reflectance distribution function (BRDF). The goal is to propose an inversion framework to retrieve surface properties, including uncertainties, in order to demonstrate the validity of the approach. In order to speed up the inversion, we based the algorithm on lookup tables that minimize the computation time of the direct model. This strategy will be very useful for analyzing real hyperspectral images. The thickness of ice estimated from the inversion is validated in comparison to real direct measurements. In addition, the specular lobe is adjusted to demonstrate that the model is able to reasonably fit the data with a coherent roughness value.

2 Description of the model

The model, from Andrieu et al. (2015), is inspired from an existing one described in Hapke (1981) and Douté and Schmitt (1998), which simulates the bidirectional reflectance of stratified granular media. It has been adapted to compact slabs, contaminated with pseudo-spherical inclusions, and a rough top interface. In the context of this work, we suppose a layer of pure slab ice, overlying an optically thick layer of granular ice, as described in Fig. 1. The roughness of the first interface is described using the probability density function of orientations of slopes defined in Hapke (1984). This distribution of orientations is fully described by a mean slope parameter $\bar{\theta}$. The ice matrix is described using its optical constants and its thickness. Within the slab, the

TCD
9, 5137–5169, 2015

model can also incorporate inclusions, assumed to be close to spherical and homogeneously distributed inside the matrix. They are described by their optical constants, their volumetric proportions and their characteristic grain sizes. There can be several different types of inclusions. Each type can be of any material but the one constituting the matrix: it can be any other kind of ice or mineral, or even bubbles.

Figure 2 illustrates the general principle of the model. The simulated bidirectional reflectance results from two separate contributions: specular and diffuse. The specular contribution of a measurement is estimated from the roughness parameter, the optical constants of the matrix, and the apertures of the light source and the detector. The surface is considered to be constituted of many unresolved facets, whose orientations follow the defined probability density function. The specular reflectance is obtained integrating every reflection on the different facets. The total reflection coefficient at the first rough interface is obtained by integrating specular contributions in every emergent direction, at a given incidence. This gives the total amount of energy transmitted into the system constituted of the contaminated slab and the substrate. The diffuse contribution is then estimated through solving the radiative transfer equation inside this system under various hypotheses. The following considerations are made. (i) The first transit through the slab is anisotropic due to the collimated radiation from the source, and that there is an isotropization at the second rough interface (i.e., when the radiation reach the semi-infinite substrate). For the refraction and the internal reflection, every following transit is considered isotropic. (ii) The geometrical optics are valid. This means that the size of the inclusions and the thickness of the slab layer must be larger than the considered wavelength. (iii) The inclusions inside the matrix are close to spherical and homogeneously distributed. The reflection and transmission factors of the layers are obtained using an analytical estimation of the Fresnel coefficients described in Chandrasekhar (1960) and Douté and Schmitt (1998), as well as a simple statistical approach, detailed in Andrieu et al. (2015). The contribution of the semi-infinite substrate is described by its single-scattering albedo. Finally, as the slab layer is under a collimated radiation from the light source, and under a diffuse radiation

TCD
9, 5137–5169, 2015

from the granular substrate, the resulting total bidirectional reflectance is computed using adding–doubling formulas.

3 Data

3.1 Spectro-radiogoniometer

The bidirectional reflectance spectra were measured using the spectro-radiogoniometer from IPAG fully described in Brissaud et al. (2004). We collected spectra in the near infrared at incidences ranging from 40 to 60°, emergence angles from 0 to 50°, and azimuth angles from 0 to 180°. The sample is illuminated with a large monochromatic beam (divergence < 1°) and the near-infrared spectrum covering the range from 0.800 to 4.800 µm is measured by an InSb photovoltaic detector. This detector has a nominal aperture of 4.2°, which results in a field of view on the sample of approximately 20 mm in diameter. The minimum angular sampling of illumination and observation directions is 0.1°, with a reproducibility of 0.002°. In order to avoid azimuthal anisotropy, the sample is rotated during the acquisition. The sample rotation axis may be very slightly misadjusted, resulting in a notable angular drift on the emergence measured up to 1°.

3.2 Ice BRDF measurements

The ice samples were obtained by sawing artificial columnar water ice into sections. These sections were put on top of an optically thick layer of compacted snow that was collected in Arselle, in the French Alps. The spectral measurements were conducted in a cold chamber at 263 K. However, the ice and the snow were unstable in the measurement's environment, due to the dryness of the chamber's atmosphere. The grain size of the snow showed an evolution, and the thickness of a given slab showed a decrease of 0.343 mm day^{-1}. Each sample needs an acquisition time of 10 h. For each measurement, the ice slab was sliced, and its thickness was measured in five different

TCD
9, 5137–5169, 2015

locations. It was then set on top of the snow sample, and this system was put into rotation in the spectro-goniometer for the measurement. As the surface is not perfectly planar, the measured thickness is not constant. This results in an 2σ standard deviation in the measurement of the thickness than ranges from 0.54 to 2.7 mm in our study, depending on the sample.

3.2.1 Specular contribution

The specular contribution was measured on a 12.51 mm thick slab sample on top of Arselle snow. This sample is described as sample 3 in the next paragraph. The illumination was at an incidence angle of 50°, and 63 different emergent geometries were sampled, ranging from 45 to 55° in emergence and from 170 to 180° in azimuth. A measure at the wavelength of 1.5 µm is shown in Fig. 5a. The sampling is 1° in emergence and azimuth within 47 and 53° in emergence and 175 and 180° in azimuth.

3.2.2 Diffuse reflectance spectra

The diffuse contribution was measured on three samples of different slab thickness. The three thicknesses were measured on different locations of the samples with a caliper before the spectro-goniometric measurement, resulting in $h_1 = 1.42 \pm 0.47$ mm, $h_2 = 7.45 \pm 0.84$ mm, $h_3 = 12.51 \pm 2.7$ mm, respectively, for samples 1, 2 and 3, with errors at 2σ. Sixty-one wavelengths were sampled ranging from 0.8 to 2.0 µm. Spectra were collected on 39 different points of the BRDF for the incidence, emergence and azimuth angles: $[40, 50, 60^\circ]$, $[0, 10, 20]$ and $[0, 45, 90, 140, 160, 180^\circ]$, respectively. This set of angles results in only 39 different geometries because the azimuthal angle is not defined for a nadir emergence.

3.2.3 Snow diffuse reflectance spectra

Diffuse reflectance spectra of natural snow only were also measured. The objective was to estimate the effect of a slab layer on the BRDF. Figure 3 shows the reflectance

TCD
9, 5137–5169, 2015

factor vs. phase angle of the snow and the snow covered with a 1.42 mm thick ice slab (sample 1). It illustrates the two most notable effects of a thin layer of slab ice on top of an optically thick layer of snow. The most intuitive effect is to lower the level of reflectance: it is due to absorption during the long optical path lengths in the compact ice matrix. The second effect is that the radiation is more Lambertian than that of snow only. These data give credit to the first hypothesis of isotropization of the radiation formulated in the model (see Sect. 2). The description of the bottom granular layer as isotropic, defined only by its single-scattering albedo, may be considered simplistic, but this data set shows that a thin coverage of slab ice, even on a very directive material such as snow, is enough to strongly flatten the BRDF.

4 Method

We designed an inversion method aimed at massive data analysis. This method consists of two steps: first, the generation of a synthetic database that is representative of the variability in the model, and then comparison with actual data. To generate the synthetic database, we used optical constants for water ice at 270 K. The 7 K difference between the actual temperature of the room and the temperature assumed for the optical constants has a negligible effect. We combined the data sets of Warren and Brandt (2008) and Schmitt et al. (1998), making the junction at 1 µm, the former set for the shorter wavelengths and the latter for the wavelengths larger than 1 µm.

In order to validate the model on the specular reflection from the slab, we chose to use the reflectance at 1.5 µm, where the ice is very absorptive. Figures 4 and 5 clearly demonstrate that there is a negligible diffuse contribution in geometry outside the specular lobe from the sample with a 12.51 mm thick pure slab. Thus, the roughness parameter $\bar{\theta}$ is the only one impacting the reflectance in the model. We chose to inverse this parameter first and validate the specular contribution.

We will then focus on the validation in the spectral domain, for the diffuse contribution. We will use the estimation of the roughness parameter $\bar{\theta}$ obtained earlier and the

TCD
9, 5137–5169, 2015

spectral data in order to estimate the slab thickness and the grain size of the snow substrate. To do this, we assume that the roughness is not changing significantly enough to have a notable impact on diffuse reflectance from one sample to another. This assumption is justified by the fact that the different columnar ice samples were made the same way, as flat as possible and the low value of $\bar{\theta}$ retrieved as discussed in the next section. It is confirmed by the results of Sect. 4.2, which suggest a very low roughness, as expected. Such low roughness parameters have negligible influence on the amount of energy injected into the surface.

4.1 Inversion strategy

The inversion consists in estimating the model parameters m from the models $F(m)$ that are close to the data d. Tarantola and Valette (1982) showed that it can be mathematically solved by considering each element as a probability density function (PDF). In non-linear direct problems, the solution may not be analytically approached. Nevertheless, it is possible to sample the solutions' PDF with a Monte Carlo approach as shown in Mosegaard and Tarantola (1995), but this solution is very time consuming.

The actual observation is considered as prior information on the data $\rho_D(d)$ in the observation space D. It is assumed to be a N-dimension Gaussian PDF $\mathcal{G}(\boldsymbol{d}_{\text{mes}}, \overline{\overline{\mathbf{C}}})$, confirmed with mean $\boldsymbol{d}_{\text{mes}}$ and covariance matrix $\overline{\overline{\mathbf{C}}}$. The values r_i are the observations for each element (angular or spectral as described later). The covariance matrix $\overline{\overline{\mathbf{C}}}$ is assumed here to be diagonal since measurements at a given geometry/wavelength are independent of the other measurements. The diagonal elements C_{ii} are $\sigma_1^2, \ldots, \sigma_N^2$, with σ_i being the standard deviations of each measurement. The prior information on model parameters $\rho_M(m)$ in the parameters space M is independent of the data and corresponds to the state of null information $\mu_D(d)$ if no information is available on the parameters. We consider a uniform PDF in their definition space M. The posterior PDF in the model space $\sigma_M(m)$ as defined by Tarantola and Valette (1982) is

TCD
9, 5137–5169, 2015

$$\sigma_{\mathrm{M}}(m) = k\rho_{\mathrm{M}}(m)L(m), \tag{1}$$

where k is a constant and $L(m)$ is the likelihood function,

$$L(m) = \int_{\mathrm{D}} \mathrm{d}d \, \frac{\rho_{\mathrm{D}}(d)\,\theta(d \mid m)}{\mu_{\mathrm{D}}(d)}, \tag{2}$$

where $\theta(d \mid m)$ is the theoretical relationship of the PDF for d given m. We do not consider errors on the model itself, so $\theta(d \mid m) = \delta(\boldsymbol{F}(\boldsymbol{m}))$ is also noted $\boldsymbol{d}_{\mathrm{sim}}$ for simulated data. So the likelihood is simplified into

$$L(m) = \mathcal{G}(\boldsymbol{F}(\boldsymbol{m}) - \boldsymbol{d}_{\mathrm{mes}}, \overline{\overline{\mathbf{C}}}), \tag{3}$$

and in the case of an uniform prior information $\rho_{\mathrm{M}}(m)$, the posterior PDF is

$$\sigma_{\mathrm{M}}(m) = kL(m). \tag{4}$$

This expression is explicitly

$$\sigma_{\mathrm{M}}(m) = k.\exp\left(-\frac{1}{2}\times^{t}(\boldsymbol{F}(\boldsymbol{m}) - \boldsymbol{d}_{\mathrm{mes}})\overline{\overline{\mathbf{C}}}^{-1}(\boldsymbol{F}(\boldsymbol{m}) - \boldsymbol{d}_{\mathrm{mes}})\right). \tag{5}$$

The factor k is adjusted to normalize the PDF. The mean value of the estimated parameter can be computed by

$$\langle m \rangle = \int_{M} m.\sigma_{\mathrm{M}}(m)\mathrm{d}m, \tag{6}$$

and the standard deviation,

TCD
9, 5137–5169, 2015

$$\sigma_{\langle m \rangle} = \int_M (m - \bar{m})^2 . \sigma_{\mathrm{M}}(m) \mathrm{d}m. \tag{7}$$

In order to speed up the inversion strategy but keep the advantage of the Bayesian approach, we choose to sample the parameter space M with regular and reasonably fine steps, noted i. The likelihood for each element is

$$L(i) = \exp\left(-\frac{1}{2} \times^t (\boldsymbol{d}_{\mathrm{sim}}(i) - \boldsymbol{d}_{\mathrm{mes}}) \overline{\overline{\mathbf{C}}}^{-1} (\boldsymbol{d}_{\mathrm{sim}}(i) - \boldsymbol{d}_{\mathrm{mes}}) \right). \tag{8}$$

The derivation of posterior PDF with such formalism for specular lobe inversion and for spectral inversion is explained in the next sections.

4.2 Specular lobe

To study the specular spot, we have to consider the whole angular sampling of the spot as single data measurement. Similar to the "pixel" (contraction of *picture element*), we choose to define the "angel" (contraction of *angular element*), as a single element in a gridded angular domain. Interestingly, angel also refers to a supernatural being represented in various forms of glowing light. A single angel measurement could not well constrain the model, even at different wavelengths. Instead a full sampling around the specular lobe should be enough, even at one single wavelength. We chose a wavelength where the diffuse contribution was negligible in order to simplify the inversion strategy. We first generated a synthetic database (lookup table), using the direct radiative transfer model. We simulated spectra in the same geometrical conditions, for a 12.5 mm thick ice layer over a granular ice substrate constituted of 1000 µm wide grains. These two last parameters are not important since the absorption is so high in ice, such that the main contribution is from the specular reflection, and the diffuse contribution is negligible.

TCD
9, 5137–5169, 2015

The sampling of the parameter space, i.e., the lookup table, must correctly represent every possible variability. For this study, we sampled the roughness parameter from 0.1 to 5° with a constant step $\mathrm{d}\bar{\theta} = 0.01°$. We use a likelihood function L defined in Eq. (8), where $\boldsymbol{d}_{\mathrm{sim}}$ and $\boldsymbol{d}_{\mathrm{mes}}$ are n_{geom}-elements vectors, with n_{geom} the number of angels (63 in this study). They respectively represent the simulated and measured reflectance at a given wavelength in every geometry. $\overline{\overline{\mathbf{C}}}$ is a $n_{\mathrm{geom}} \times n_{\mathrm{geom}}$ matrix. It represents the uncertainties in the data. In this case, we considered each wavelength independently, thus generating a diagonal matrix, containing the level of errors given by the technical data of the instrument described by Brissaud et al. (2004). The roughness parameter $\bar{\theta}$ returned by the inversion will be described by its normalized PDF:

$$\mathcal{P}\left\{\bar{\theta}(i)\right\} = \frac{L(i)\,\mathrm{d}\bar{\theta}}{\sum_j L(j)\,\mathrm{d}\bar{\theta}} = \frac{L(i)}{\sum_j L(j)}. \tag{9}$$

The best match is the value $\bar{\theta}(i)$ with the highest probability. The full PDF can be estimated by its mean,

$$\left\langle\bar{\theta}\right\rangle = \frac{\sum_i \bar{\theta}(i) L(i)}{\sum_i L(i)}, \tag{10}$$

and associated standard deviations,

$$\sigma_{\langle\bar{\theta}\rangle} = \sqrt{\frac{\sum_i \left(\bar{\theta}(i) - \left\langle\bar{\theta}\right\rangle\right)^2 L(i)}{\sum_i L(i)}}. \tag{11}$$

We give error bars on the results that correspond to two standard deviations, and thus a returned value for $\bar{\theta}$ that is

$$\bar{\theta}_r = \left\langle\bar{\theta}\right\rangle \pm 2\sigma_{\langle\bar{\theta}\rangle}. \tag{12}$$

TCD
9, 5137–5169, 2015

4.3 Diffuse spectra

When out of the specular spot, the radiation is controlled by the complex transfer through the media (slab ice and bottom snow). The experimental samples were made of pure water slab ice, without impurity. We generated the lookup table for every measurement geometry at very high spectral resolution (4.10^{-2} nm) as required by the variability in the optical constants of water ice, and then down-sampled it at the resolution of the instrument (2 nm). We sampled the 17 085 combinations of two parameters for the 39 different geometries: p_1 the thickness of the slab from 0 to 20 mm (noted $i = [1,201]$) every 0.1 mm (noted $\mathrm{d}p_1$), and p_2 the grain size of the granular substrate from 2 to 25 µm every 1 µm and from 25 to 1500 µm every 25 µm (noted $j = [1,85]$ and the corresponding $\mathrm{d}p_2(j)$). The parameters space is thus irregularly paved with $\mathrm{d}p(i,j) = \mathrm{d}p_1.\mathrm{d}p_2(j)$.

For the inversion, we used the same method as previously described, with a likelihood function L that is written as in Eq. (8). Two different strategies were adopted. First, we inverted each spectra independently. Thirty-nine geometries were sampled (described in Sect. 3.2), and thus we conducted 39 inversions for each sample. This time $\boldsymbol{d}_{\mathrm{sim}}$ and $\boldsymbol{d}_{\mathrm{mes}}$ are thus respectively the simulated and measured spectra. Then $\boldsymbol{d}_{\mathrm{sim}}$ and $\boldsymbol{d}_{\mathrm{mes}}$ are n_{b}-elements vectors, where n_{b} is the number of bands (61 in this study) and $\overline{\overline{\mathbf{C}}}$ is a $n_{\mathrm{b}} \times n_{\mathrm{b}}$ matrix. As previously (see Sect. 4.2), we considered each wavelengths independently, thus generating a diagonal matrix, containing the level of errors given by the technical data of the instrument given by Brissaud et al. (2004). The error is a percentage of the measurement, and thus $\overline{\overline{\mathbf{C}}}$ will be different for every inversion.

Secondly, we inverted the BRDF as a whole, for each sample. For this method, $\boldsymbol{d}_{\mathrm{sim}}$ and $\boldsymbol{d}_{\mathrm{mes}}$ are respectively the simulated and measured BRDF and are thus $n_{\mathrm{b}} \times n_{\mathrm{geom}}$-elements vectors (2379 in this study), where n_{b} is the number of bands (61 in this study) and n_{geom} is the number of geometries (39 in this study) sampled.

TCD
9, 5137–5169, 2015

$\overline{\overline{\mathbf{C}}}$ is a $\left(n_b \times n_{geom}\right) \times \left(n_b \times n_{geom}\right)$ diagonal matrix, containing the errors on the data. We represent the results the same way as previously, but there are two parameters to inverse. For the sake of readability, we plot the normalized marginal probability density function for each parameter. We present here the general method for the inversion of $n_p = 2$ parameters: the slab thickness and the grain size of the substrate. The PDF for the two parameters p is described by

$$\mathcal{P}\{p(i,j)\} = \frac{L(i,j)\,\mathrm{d}p(i,j)}{\sum_i \sum_j L(i,j)\,\mathrm{d}p(i,j)}. \tag{13}$$

For a given parameter p_1, the marginal PDF of the solution is

$$\mathcal{P}\{p_1(i)\} = \frac{L'(i)\,\mathrm{d}p_1(i)}{\sum_i \sum_j L(i,j)\,\mathrm{d}p(i,j)}, \tag{14}$$

with $L'(i) = \sum_j L(i,j)\mathrm{d}p_2(j)$. The best match is the value $p_1(i)$ with the highest probability. The marginal PDF can be described by the mean,

$$\langle p_1 \rangle = \frac{\sum_i p_1(i) L'(i)\,\mathrm{d}p_1(i)}{\sum_i \sum_j L(i,j)\,\mathrm{d}p(i,j)}, \tag{15}$$

and the associated standard deviation,

$$\sigma_{\langle p_1 \rangle} = \sqrt{\frac{\sum_i \left(p_1(i) - \langle p_1 \rangle\right)^2 L'(i)\,\mathrm{d}p_1(i)}{\sum_i \sum_j L(i,j)\,\mathrm{d}p(i,j)}}. \tag{16}$$

As for the roughness parameter, we give error bars on the results that correspond to two standard deviations, and thus a returned value for p_1 that is

$$p_{1r} = \langle p_1 \rangle \pm 2\sigma_{\langle p_1 \rangle}. \tag{17}$$

TCD
9, 5137–5169, 2015

5 Results

5.1 Specular lobe

We performed the inversion taking into account 63 angel measurements, but for the sake of readability, Fig. 4 represents only the reflectance in the principle plane. The shapes and the intensities in Fig. 4a are compatible, but the measurement and simulation are not centered at the same point. The simulation is centered at the geometrical optics specular point (emergence 50° and azimuth 180°), whereas the measurement seems to be centered around an emergence of 50.5°. This could be due to slight misadjustment of the rotation axis of the sample in the instrument. This kind of misadjustment is common, and can easily result in a notable shift up to 1° of the measure. We simulated different possible shifts in this range, and found a best match represented in Fig. 4b for a shift of 0.5° in emergence, as was suggested by the first plot in Fig. 4a, and 0.2° in azimuth. The measurements and the best match are represented in Fig. 5. The shape and the magnitude of the specular lobe are very well reproduced. Both lobes show a small amount of asymmetry forward. This asymmetry is not due to the sampling as it is also present when the simulation is not shifted (see the red curve in Fig. 4). It is due to an increase in the Fresnel reflection coefficient when the phase angle increases for this range of geometries. Figure 6 shows the PDF a posteriori for the parameter $\bar{\theta}$. The best match was obtained with $\bar{\theta} = 0.43°$. The inversion method gives a result with a close to Gaussian shape at $\bar{\theta} = 0.424° \pm 0.046°$. Unfortunately, we have no direct measurements of $\bar{\theta}$. It would require a digital terrain model of the sample that is difficult to obtain in icy samples. Still, we find a low value, which is consistent with the production in laboratory of slabs of columnar ice that are very flat, but still imperfect as described in the data set. The average slope is compatible with a long-wavelength slope at the scale of the sample, demonstrating that the micro-scale was not important in our case. Indeed, for a sample that has a length L, a 1σ standard deviation on the thickness Δh can be attributed to a general slope $\vartheta = \arctan\left(\frac{\Delta h}{L}\right)$ due to a small error in the parallelism of the two surfaces of the slab. In the case of sample 3, $L = 20\,\mathrm{cm}$

TCD
9, 5137–5169, 2015

and $\Delta h = 1.35\,\mathrm{mm}$ result in $\vartheta = 0.39^{\circ}$, which is compatible with the roughness given by the inversion. We thus think that what we see is an apparent roughness due to a small general slope on the samples, and that the roughness at the surface is much lower than this value.

Moreover, the value retrieved by the inversion is very well constrained as the probability density function is very sharp. This means that we have an a posteriori uncertainty on the result that is very low. The quality of the reproduction of the specular spot by the model suggests that the surface slope description is a robust description despite its apparent simplicity. In particular, one single slope parameter is enough to describe this surface.

5.2 Diffuse

To reproduce diffuse reflectance we used the results obtained with the specular measurements and assumed that the roughness of the samples was not changing much between the experiments. The range of variations in roughness should be negligible in the spectral analysis. We simulated slabs over snow, having the grain size of the substrate and the thickness of the slab as free parameters. Figure 7 represents examples of the best matches we obtained for the three measured samples at various geometries. We also represented the mismatch between the best fits and the observations. We find an agreement between the data and the model that is acceptable. Nevertheless, there seems to be a decrease in quality in the fits as the thickness increases. Figure 8 shows an example of the marginal PDF for the three samples that are associated with the previous fits. The thickness is well constrained as the marginal probability density functions a posteriori are relatively sharp and very close to Gaussian. However, the grain size of the substrate seems to have a limited impact on the result since it is little constrained. The marginal PDFs for the grain size of the substrate are broad, and thus the a posteriori relative uncertainties in the result are very high. Unfortunately, we have no reliable measurement of the grain size of the substrate, as it is evolving during

TCD
9, 5137–5169, 2015

the time of the measurements. The general trend of decreasing grain size seems to be in agreement with visual assessment.

Figure 9 shows the measurements and the final result of the inversion of the thickness for the three samples, and for 39 measurement geometries independently. The data and the model are compatible. Still, the thickness of sample 1 is slightly overestimated. This may reveal a sensitivity limit of the model. The thickness of sample 3 seems underestimated. This could be partly due to the duration of the measurement: the slab sublimates as the measure is being taken. Moreover, the specular measurements were performed on that sample, increasing even more the duration of the experiment. The inversions points in Fig. 9 are sorted by increasing incidence and, for each incidence, by increasing azimuth. There seems to be an influence of the geometry on the returned result: it is particularly clear for sample 2. The estimated thickness tends to increase with incidence and decrease with azimuth. This effect disappears for large thicknesses (sample 3). Figure 10 shows the measure and the best match at the $\lambda = 1.0\,\mu m$ wavelength when conducting the inversion on the whole BRDF data set for each sample. The relatively flat behavior of the radiation with the phase angle is reasonably well reproduced. The quality of the geometrical match increases with the thickness of the sample. This is consistent with the fact that a thicker slab will permit a stronger isotropization of the radiation. It is also consistent with the disappearance of the geometrical dependence on the estimation for large thicknesses noted in Fig. 9. The values of thicknesses returned by the inversion are displayed in Fig. 11a: they are also compatible with the data, and the results are close to the one given by independent inversions on each geometry (see Figs. 8 and 9). The grain sizes returned, even if compatible with the independent inversion results, are at the boundary of the definition range of the parameter for samples 2 and 3. This means that the model cannot estimate this parameter correctly. Indeed, as displayed in Fig. 11, the a posteriori marginal PDFs for samples 2 and 3 are very close to a Dirac delta function at the lower limit of the domain. This means that the model inversion process cannot fit a value for this parameter inside the definition domain that is fully satisfying. This suggests an evo-

TCD
9, 5137–5169, 2015

lution of the conditions of the experiment between the measure for sample 1 and the others. The fact that the returned value is at the lower boundary of the grain-size range suggests that the actual grain size of the snow is lower than this value. Unfortunately, such a grain size would contradict the fundamental hypothesis of geometrical optics assumed by the model. These results shall thus be interpreted as grain sizes smaller than the limit of detection. This kind of very small grain size could be produced during the experiments by a small temperature difference between the slabs and the natural snow, resulting in the condensation of frost at the bottom of the slab layer.

6 Discussion and conclusion

The aim of this present work is to validate an approximate radiative transfer model developed in Andrieu et al. (2015) using several assumptions. The most debated one is the isotropization of the radiation when it reaches the substrate. We first qualitatively validated this assumption with snow and ice data. We then quantitatively tested and validated our method using a pure slab ice with various thickness and snow as a bottom condition. The thicknesses retrieved by the inversion are compatible with the measurements for every geometry, demonstrating the robustness of this method to retrieve the slab thickness from spectroscopy only. The result given by the inversion of the whole data set is also compatible with the measurements.

We also validate the angular response of such slabs in the specular lobe. Unfortunately, it was not possible to measure the micro-topography in detail to compare with the retrieved data. Nevertheless, we found a very good agreement between the simulation and the data. The average slope is compatible with a long-wavelength slope at the scale of the sample, demonstrating that the micro-scale was not important in our case. This is probably due to the sharp slicing method used. In future work, an experimental validation of the specular lobe and roughness should be addressed.

The large uncertainties in the grain size inversion demonstrate that the bottom condition is less important than the slab for the radiation field at first order, as expected.

TCD
9, 5137–5169, 2015

Even at a thickness of 1.4 mm, since water ice is highly absorbent, the bottom layer is difficult to sense.

In Fig. 7, there seems to be a decrease in the quality of the fit when the slab thickness increases. We explain it by the order in which the experiments were conducted. Indeed, the first measurement was on the thinnest slab and the last on the thickest. During that time, the snow substrate was sublimating. The errors in the fits could be due to the increasing contamination in the substrate. The natural snow cannot be perfectly pure: as it sublimates during the measurements, the contribution of the contaminants becomes stronger and stronger. These contaminants are not known and are not taken into account in the model. A way to avoid this problem could be to set the slab ice on top of a non-volatile granular material, such as dry mineral sand, whose optical constants are known or can be determined. However this would not solve another problem, which is the re-condensation of water into frost between the granular substrate and the slab.

The comparison of the a posteriori uncertainties in the thickness of the slab and the grain size of the snow substrate illustrates the fact that those uncertainties depend both on the constraint brought by the model itself and the uncertainty introduced into the measurement, which only the Bayesian approach can handle. The use of Bayesian formalism is thus very powerful in comparison with traditional minimization techniques.

We propose here a fast and innovative inversion method aiming at massive inversion, for instance for remote sensing spectro-imaging data, that enables accurate estimation of the uncertainties in the model's parameters. As an example, the lookup tables used for this project were computed in ~ 150 s for the roughness study (1763 wavelengths sampled, 30 933 spectra) and ~ 2.5 h for the thickness and grain size study (33 186 wavelengths sampled, 666 315 spectra). The inversions themselves were performed in less than one-tenth of a second for specular lobe and independent spectral inversions, and 2 s for BRDF-as-a-whole inversions. Every calculation was computed on one Intel CPU with 4 GB RAM. It has to be noted that once the lookup table has been created, an unlimited number of inversions can be conducted. The model is fast and the inversion is highly parallel and thus adapted to the study of the compact ice-covered surfaces of

TCD
9, 5137–5169, 2015

the solar system. For inversions over very large databases, the code has been adapted to GPU parallelization. It is also possible to increase the speed of the calculation of the lookup tables by means of multi-CPU computing.

References

Andrieu, F., Douté, S., Schmidt, F., and Schmitt, B.: Radiative transfer model for contaminated rough slabs, ArXiv e-prints, Appl. Optics, accepted, 2015. 5138, 5140, 5141, 5154, 5160

Appéré, T., Schmitt, B., Langevin, Y., Douté, S., Pommerol, A., Forget, F., Spiga, A., Gondet, B., and Bibring, J.-P.: Winter and spring evolution of northern seasonal deposits on Mars from OMEGA on Mars Express, J. Geophys. Res.-Planet., 116, E05001, doi:10.1029/2010JE003762, 2011. 5139

Brissaud, O., Schmitt, B., Bonnefoy, N., Douté, S., Rabou, P., Grundy, W., and Fily, M.: Spectrogonio radiometer for the study of the bidirectional reflectance and polarization functions of planetary surfaces. 1. Design and tests, Appl. Optics, 43, 1926–1937, 2004. 5138, 5142, 5148, 5149

Carmagnola, C. M., Domine, F., Dumont, M., Wright, P., Strellis, B., Bergin, M., Dibb, J., Picard, G., Libois, Q., Arnaud, L., and Morin, S.: Snow spectral albedo at Summit, Greenland: measurements and numerical simulations based on physical and chemical properties of the snowpack, The Cryosphere, 7, 1139–1160, doi:10.5194/tc-7-1139-2013, 2013. 5139

Chandrasekhar, S.: Radiative Transfer, Dover, New York, 1960. 5141

Douté, S., and Schmitt, B.: A multilayer bidirectional reflectance model for the analysis of planetary surface hyperspectral images at visible and near-infrared wavelengths, J. Geophys. Res., 103, 31367–31389, doi:10.1029/98JE01894, 1998. 5140, 5141

Dozier, J., Green, R. O., Nolin, A. W., and Painter, T. H.: Interpretation of snow properties from imaging spectrometry, Remote Sens. Environ., 113, Supplement 1, S25–S37, 2009. 5139

Dumont, M., Brissaud, O., Picard, G., Schmitt, B., Gallet, J.-C., and Arnaud, Y.: High-accuracy measurements of snow Bidirectional Reflectance Distribution Function at visible and NIR wavelengths – comparison with modelling results, Atmos. Chem. Phys., 10, 2507–2520, doi:10.5194/acp-10-2507-2010, 2010. 5139

TCD
9, 5137–5169, 2015

Dumont, M., Brun, E., Picard, G., Michou, M., Libois, Q., Petit, J.-R., Geyer, M., Morin, S., and Josse, B.: Contribution of light-absorbing impurities in snow to Greenland's darkening since 2009, Nat. Geosci., 7, 509–512, doi:10.1038/ngeo2180, 2014. 5139

Eluszkiewicz, J. and Moncet, J.-L.: A coupled microphysical/radiative transfer model of albedo and emissivity of planetary surfaces covered by volatile ices, Icarus, 166, 375–384, 2003. 5139

Eluszkiewicz, J., Moncet, J.-L., Titus, T. N., and Hansen, G. B.: A microphysically-based approach to modeling emissivity and albedo of the martian seasonal caps, Icarus, 174, 524–534, 2005. 5139

Hapke, B.: Bidirectional reflectance spectroscopy: 1. Theory, J. Geophys. Res., 86, 3039–3054, doi:10.1029/JB086iB04p03039, 1981. 5139, 5140

Hapke, B.: Bidirectional reflectance spectroscopy: 3. Correction for macroscopic roughness, Icarus, 59, 41–59, 1984. 5140

Kieffer, H. H. and Titus, T. N.: TES mapping of Mars' north seasonal cap, Icarus, 154, 162–180, 2001. 5139

Leighton, R. B. and Murray, B. C.: Behavior of carbon dioxide and other volatiles on Mars, Science, 153, 136–144, 1966. 5139

Lhermitte, S., Abermann, J., and Kinnard, C.: Albedo over rough snow and ice surfaces, The Cryosphere, 8, 1069–1086, doi:10.5194/tc-8-1069-2014, 2014. 5139

Mary, A., Dumont, M., Dedieu, J.-P., Durand, Y., Sirguey, P., Milhem, H., Mestre, O., Negi, H. S., Kokhanovsky, A. A., Lafaysse, M., and Morin, S.: Intercomparison of retrieval algorithms for the specific surface area of snow from near-infrared satellite data in mountainous terrain, and comparison with the output of a semi-distributed snowpack model, The Cryosphere, 7, 741–761, doi:10.5194/tc-7-741-2013, 2013. 5139

Mosegaard, K. and Tarantola, A.: Monte Carlo sampling of solutions to inverse problems, J. Geophys. Res., 100, 12431–12447, doi:10.1029/94JB03097, 1995. 5145

Negi, H. S. and Kokhanovsky, A.: Retrieval of snow albedo and grain size using reflectance measurements in Himalayan basin, The Cryosphere, 5, 203–217, doi:10.5194/tc-5-203-2011, 2011. 5139

Painter, T. H. and Dozier, J.: The effect of anisotropic reflectance on imaging spectroscopy of snow properties, Remote Sens. Environ., 89, 409–422, 2004. 5139

TCD
9, 5137–5169, 2015

Picard, G., Arnaud, L., Domine, F., and Fily, M.: Determining snow specific surface area from near-infrared reflectance measurements: numerical study of the influence of grain shape, Cold Reg. Sci. Technol., 56, 10–17, 2009. 5139

Pilorget, C., Vincendon, M., and Poulet, F.: A radiative transfer model to simulate light scattering in a compact granular medium using a Monte Carlo approach: validation and first applications, J. Geophys. Res.-Planet., 118, 2488–2501, doi:10.1002/2013JE004465, 2013. 5139

Schmitt, B., Quirico, E., Trotta, F., and Grundy, W. M.: Optical properties of ices from UV to infrared, in: Solar System Ices, vol. 227 of Astrophysics and Space Science Library, edited by: Schmitt, B., de Bergh, C., and Festou, M., Kluwer Academic Publishers, Dordrecht, 1199–240, 1998. 5144

Shkuratov, Y., Starukhina, L., Hoffmann, H., and Arnold, G.: A model of spectral albedo of particulate surfaces: implications for optical properties of the Moon, Icarus, 137, 235–246, doi:10.1006/icar.1998.6035, 1999. 5139

Stamnes, K., Tsay, S.-C., Wiscombe, W., and Jayaweera, K.: Numerically stable algorithm for discrete-ordinate-method radiative transfer in multiple scattering and emitting layered media, Appl. Optics, 27, 2502–2509, 1988. 5139

Tarantola, A. and Valette, B.: Inverse problems – quest for information, J. Geophys., 50, 150–170, 1982. 5145

Warren, S. G. and Brandt, R. E.: Optical constants of ice from the ultraviolet to the microwave: a revised compilation, J. Geophys. Res., 113, D14220, doi:10.1029/2007JD009744, 2008. 5144

Zent, A. P., McKay, C. P., Pollack, J. B., and Cruikshank, D. P.: Grain metamorphism in polar nitrogen ice on Triton, Geophys. Res. Lett., 16, 965–968, doi:10.1029/GL016i008p00965, 1989. 5139

TCD
9, 5137–5169, 2015

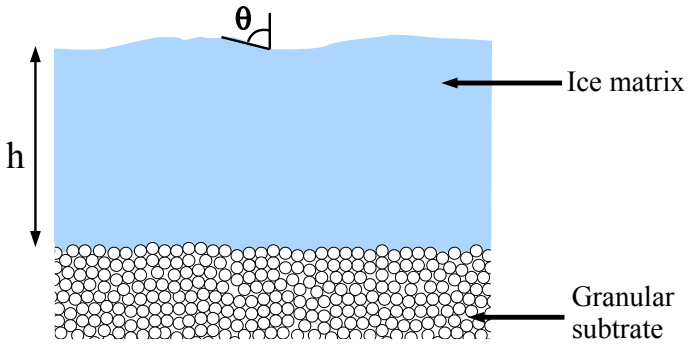

Figure 1. Scheme of the surface representation in the radiative transfer model applied to the laboratory measurements. *h* represents the slab thickness and $\bar{\theta}$ represents the mean slope to describe the surface roughness.

TCD
9, 5137–5169, 2015

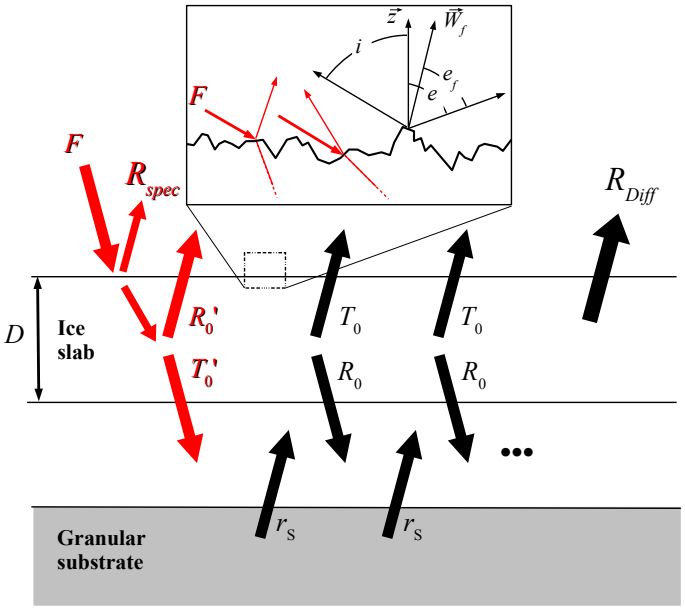

Figure 2. Illustration of the radiative transfer in the surface. Anisotropic transits are represented in red. F is the incident radiation flux, R_{spec} and R_{Diff} are respectively the specular and diffuse contributions to the reflectance of the surface, r_s is the Lambertian reflectance of the granular substrate, and R_0 and T_0 are respectively the total reflection and transmission factors of the slab layer. A prime indicates an anisotropic transit. The reflection and transmission factors are different in the cases of isotropic or anisotropic conditions. The granular and slab layers are artificially separated in this figure to help the understanding of the coupling between the two layers. Top: illustration of the reflections and transmission at the first interface, used in the calculations of R_{spec} and the determination of the amount of energy injected into the surface. z is the normal to the surface, $\boldsymbol{W}_f$ the local normal to a facet, i and e are respectively the incidence and emergence angle, and e_f is the local emergence angle for a facet. Each different orientation of a facet will lead to a different transit length in the slab. A more detailed description can be found in Andrieu et al. (2015).

TCD
9, 5137–5169, 2015

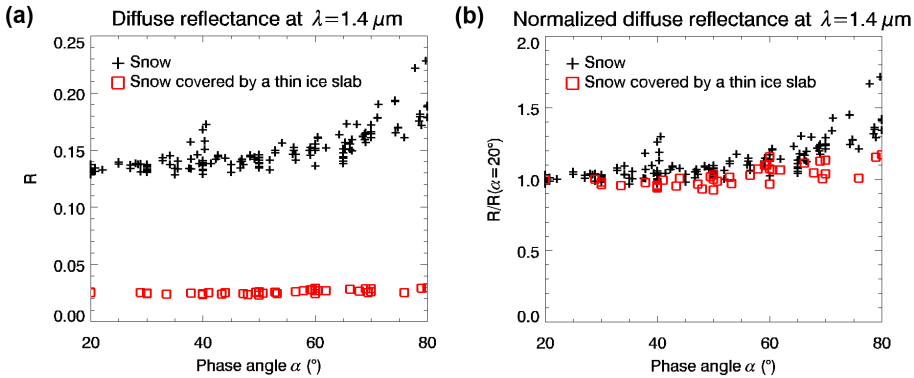

Figure 3. (a) Reflectance factor at a wavelength of $\lambda = 1.4\,\mu m$ vs. phase angle for snow only (black crosses) and the same snow but covered with a $1.42 \pm 0.27\,mm$ water ice slab (red squares). The thin layer of slab ice not only lowers the level of reflectance as expected but also seems to isotropize the reflected radiation. This is clearer on plot **(b)**, which represents the same data but normalized by the value at a phase angle $\alpha = 20^{\circ}$. This data shows that even a very thin layer of ice has a strong effect on the directivity of the surface. This justifies the approximation of isotropization at the second interface supposed by the model, and the description of the substrate using only its single-scattering albedo.

TCD
9, 5137–5169, 2015

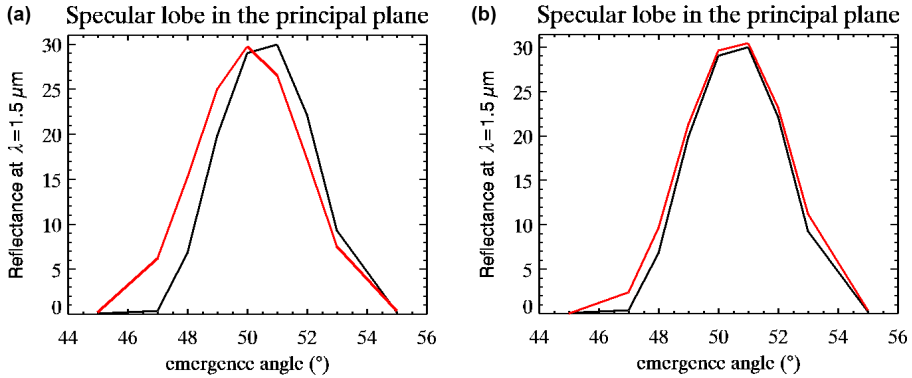

Figure 4. (a) Measured (black) and simulated (red) reflectance at 1.5 µm in the principal plan for an incidence angle of 50°. The specular lobe measured is not centered at 50°. The sample may be slightly misadjusted resulting in a general drift on the observation. **(b)** Measured (black) and simulated (red) reflectance at 1.5 µm in the principal plan for an incidence angle of 50°. We simulated a small misadjustment of the sample, resulting in a shift of the observation of 0.5° in emergence and 0.2° in azimuth. With this adjustments, the model reproduces the data well.

TCD
9, 5137–5169, 2015

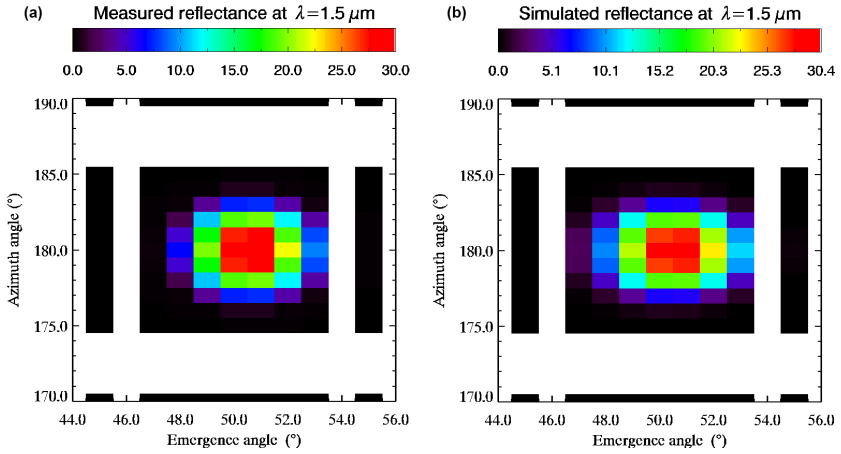

Figure 5. Measured and simulated reflectance around the specular geometry at 1.5 µm for an incidence angle of 50°. The simulation was computed assuming the determined shift of 0.5° in emergence and 0.2° in azimuth. The shape and the intensity of the specular lobe are well reproduced.

TCD
9, 5137–5169, 2015

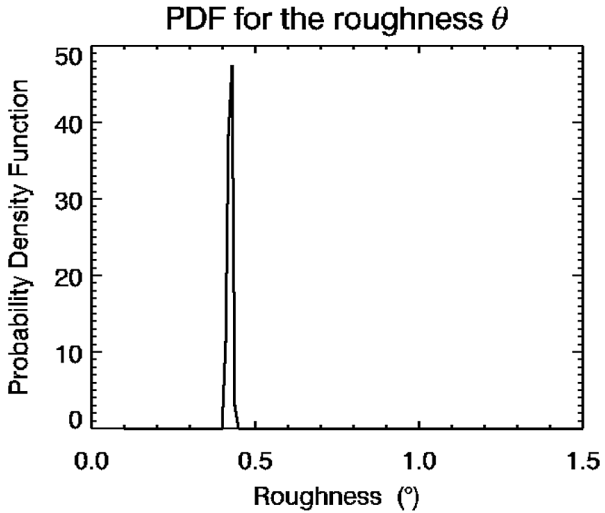

Figure 6. Probability density function a posteriori for the roughness parameter $\bar{\theta}$, noted $\mathcal{P}\{\bar{\theta}\}$. This function is very sharp and thus the parameter $\bar{\theta}$ is well constrained. The inverted value at 2σ is $\bar{\theta} = 0.424 \pm 0.046^{\circ}$. The best match is obtained for $\bar{\theta} = 0.43^{\circ}$.

TCD
9, 5137–5169, 2015

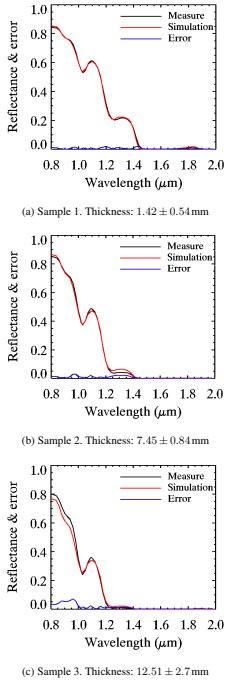

Figure 7. Measured and best match of simulated reflectance spectra for the geometry of the best match for each sample: at incidence 40°, emergence 10° and azimuth 140° for sample 1 **(a)**; at incidence 40°, emergence 20° and azimuth 45° for sample 2 **(b)**; and at incidence 60° and emergence 0° for sample 3 **(c)**. The thicknesses indicated in the captions were measured before putting the sample into the spectro-goniometer, and the errors are given at 2σ. The absolute differences are shown in blue on each graph. The simulated spectra well reproduce the data within the range of a priori uncertainties. For sample 3 **(c)**, the reflectances in the 0.8–1.0 µm range are not very well reproduced. The model cannot match the high levels of the measurement. This could be explained by a change in the experimental protocol, leading to the condensation of very fine frost at the bottom of the slab layer.

TCD
9, 5137–5169, 2015

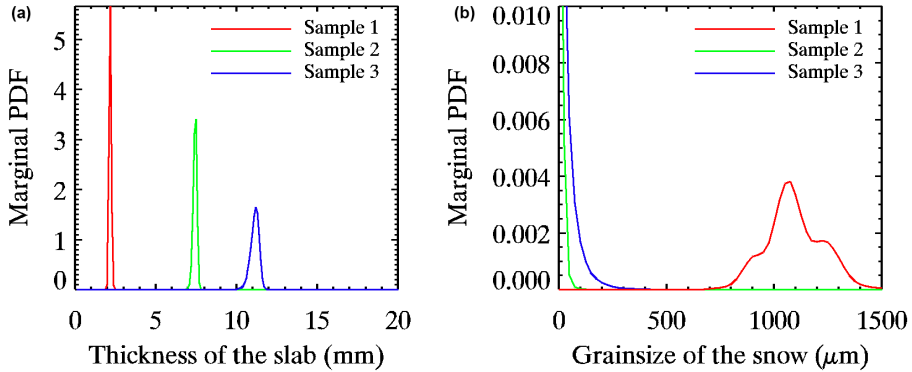

Figure 8. Marginal probability density functions a posteriori for **(a)** the thickness of the slab $\mathcal{P}\{p_1(i)\}$ and **(b)** the grain size of the snow substrate $\mathcal{P}\{p_2(j)\}$ for the three samples, and for the geometries described in Fig. 7. The functions are very sharp and very close to Gaussian for the thickness of the slab **(a)** but are broad for the grain size of the substrate **(b)**. The thickness is well constrained by the inversion, whereas the grain size of the substrate cannot be determined with high precision.

TCD
9, 5137–5169, 2015

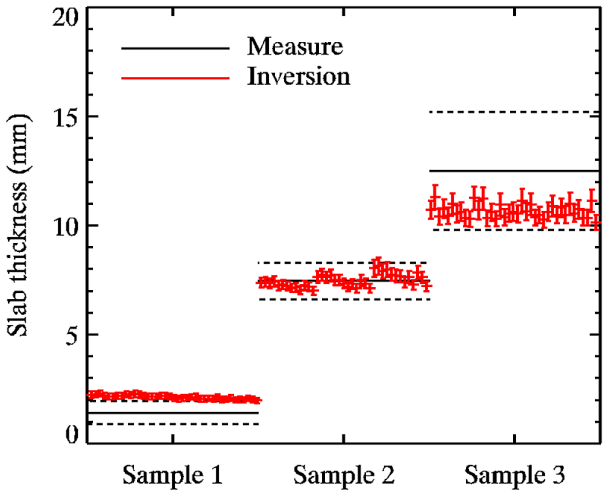

Figure 9. Results of the inversions and measures with error bars at 2σ for samples 1, 2 and 3, and for the 39 different geometries of measurement. The thicknesses retrieved and measured are compatible. The inversion points (in red) are sorted by incidence (3 values), and each incidence is then sorted by azimuth (13 values: 1 for emergence 0° and 6 each for the 10 and 20° emergences). The geometry appears to have an impact on the result for sample 1 and 2. The thickness estimated seems to increase with incidence and decrease with azimuth. The geometrical effect disappears for large thicknesses.

TCD
9, 5137–5169, 2015

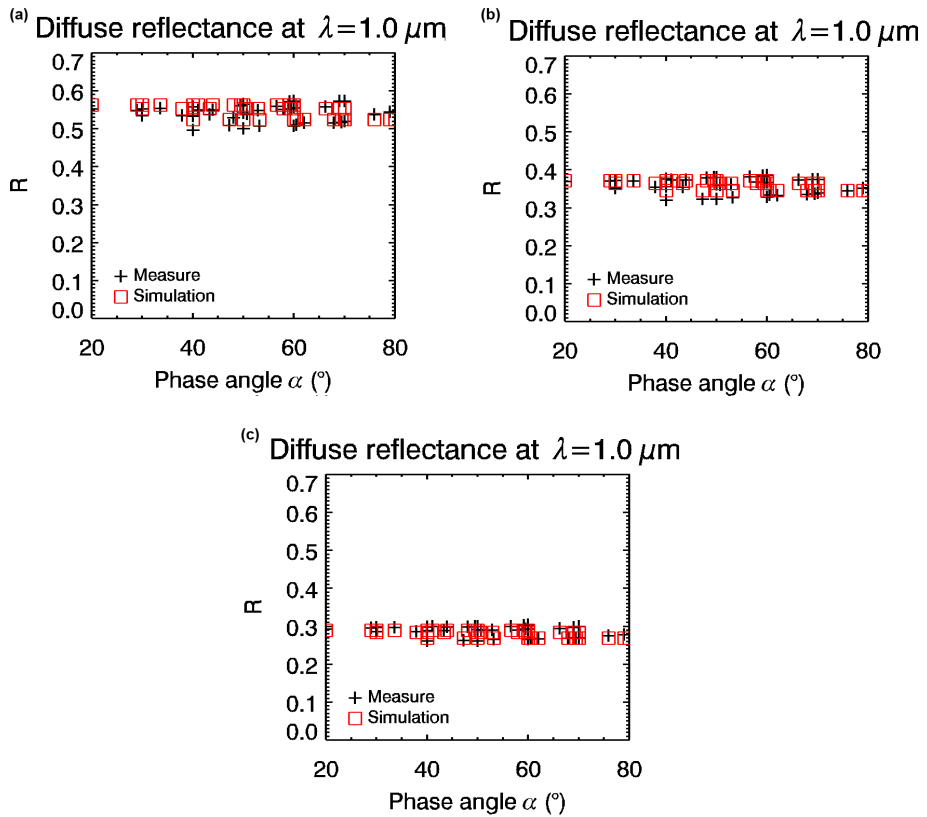

Figure 10. Measured and simulated reflectance factor at λ = 1 µm for **(a)** sample 1, **(b)** sample 2 and **(c)** sample 3. The simulation reasonably well reproduces, if not perfectly, the geometrical behavior of the surfaces. The quality of the geometrical simulation seems to increase with the thickness of the slab. This is consistent with the isotropization effect of a slab, which will increase with the thickness.

TCD
9, 5137–5169, 2015

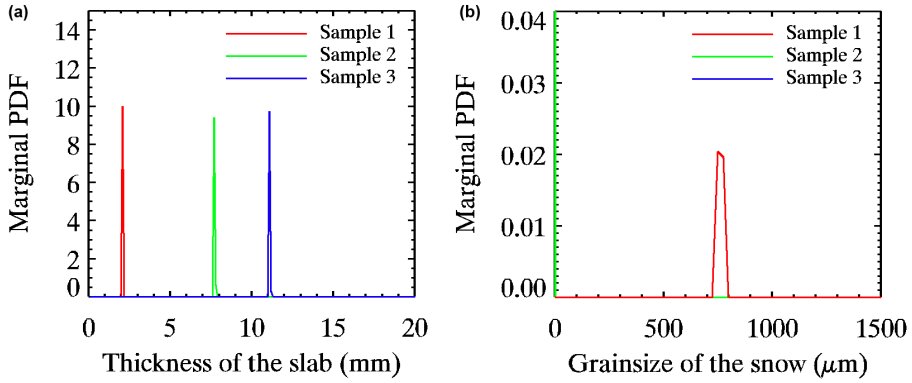

Figure 11. Marginal probability density functions a posteriori for **(a)** the thickness of the slab $\mathcal{P}\{p_1(i)\}$ and **(b)** the grain size of the snow substrate $\mathcal{P}\{p_2(j)\}$ for the three samples. The functions are very sharp and very close to Gaussian for the thickness of the slab **(a)**. The a posteriori uncertainties in the results are much smaller than the previous ones, because the data set is larger and thus more constraining. Still, these uncertainties are not fully reliable, as the model cannot perfectly reproduce the BRDF within the a priori uncertainties (see Fig. 10). **(b)** The grain size can be determined on sample 1, and is consistent with the results on inversions of single spectra (see Fig. 8). However, they cannot be inverted for sample 2 and 3, as the returned probability density function is close to a Dirac delta function at the boundary of the definition range.

TCD
9, 5137–5169, 2015